Exploring the Dirac nature of RbBi$_2$

Sharon S. Philip [1], S. Liu [2], Jeffrey C. Y. Teo [1], P. V. Balachandran [2,3] and Despina Louca [1,*]

[1]*Department of Physics, University of Virginia, Charlottesville, Virginia 22904, USA*

[2]*Department of Materials Science and Engineering, University of Virginia, Charlottesville, Virginia 22904, USA*

[3]*Department of Mechanical and Aerospace Engineering, University of Virginia, Charlottesville, Virginia 22904, USA*

Characteristics of topological semimetals such as a nonsaturating magnetoresistance (MR), a field-induced metal to semiconducting crossover and a robust resistivity plateau are observed under a magnetic field in type-I RbBi$_2$ bulk superconductor with $T_c = 4.15$ K. The MR exhibits a notable 3500% increase at 2 K and 9 T and the resistivity follows a power law temperature dependence, while the MR $\propto H^{1.26}$, indicating weak carrier compensation. First principles calculations provided insights into the dynamical stability of the cubic structure at 0 K. Both hole and electron pockets are observed at the Fermi surface. The electron-phonon interaction constant indicates weak coupling strength (<1) that leads to a maximum predicted T_c of 2.852 K. Just below the Fermi level, E$_F$, the electronic band structure consists of linear band crossings at the X points in the Brillouin zone (BZ) corresponding to massless, symmetry-protected Dirac fermions.

I. INTRODUCTION

In topological materials, the quantum state is entangled to an extent where it's emergent quasiparticles exhibit exotic behaviors that are unique and cannot be reproduced in conventional solids. These exotic properties are topologically protected as they are robust against perturbations. Studies on numerous materials to date have established that topological phases supporting topologically protected boundary states can exist in two and three dimensional time-reversal symmetry (TRS) invariant systems in the absence of an external magnetic field [1]. Many candidate topological insulators containing bismuth, Bi, have been explored for this purpose [2]. Bi metal exhibits strong spin-orbit coupling (SOC) that has been linked to topologically nontrivial band structures in its compounds. Several binary Bi compounds have been investigated for topological superconductivity. Examples include Bi-alkali and alkaline-earth intermetallic compounds such as LiBi, NaBi, KBi$_2$ [3], CsBi$_2$ [4], Ca$_{11}$Bi$_{10-x}$ [5], CaBi$_2$ [6], CaBi$_3$, SrBi$_3$ [7], BaBi$_3$ [7], and Ba$_2$Bi$_3$ [8]. Among these, KBi$_2$ [9] and CaBi$_2$ are reportedly type-I superconductors, although the topological nature of their superconductivity has not been confirmed.

RbBi$_2$ is isostructural to KBi$_2$ with a higher superconducting transition temperature, $T_c = 4.15$ K. In this work, we report on the Dirac (semi)metallic nature of RbBi$_2$ and its electronic properties. This is a superconducting system which exhibits extremely large nonsaturating MR and a Dirac dispersion. RbBi$_2$ exhibits a very large MR of about 3500% under an applied magnetic field of 9 T. While metallic behavior is observed at zero field above T_c, a metal-semiconductor crossover appears at low temperatures when the magnetic

field exceeds H$_c$. A robust resistivity plateau appears below 10 K and persists up to 9 T. These characteristics are typical of topological semimetals with centrosymmetric crystal structures [10]. At constant field, the resistivity follows a power law temperature dependence [11] while the MR is fit following Kohler's rule with an exponent, m $\sim$1.26. An m $\sim$2 is indicative of perfect carrier compensation [12], thus the current value obtained for RbBi$_2$ indicates weak carrier compensation. Phonon calculations based on first principles density functional theory (DFT) predicted the cubic structure to be dynamically stable at 0 K. The linear-response approach provided a weak electron-phonon coupling strength of < 1, yielding a maximum superconducting T_c of 2.852 K using the McMillan formula [13]. The electronic band structure near the Fermi energy showed a linear band dispersion and crossing indicative of a massless Dirac fermion at each of the three X points in the BZ below E$_F$. The massless Dirac spectrum is protected by the fourfold screw rotation symmetry S_4.

II. RESULTS AND DISCUSSION

A. Magneto-transport characterization

RbBi$_2$ is cubic with $Fd\bar{3}m$ space group symmetry [14]. The crystal structure is shown in Fig. 1(a). The Bi tetrahedra connect with each other by vertex-sharing to form a three-dimensional network and the Rb atoms are arranged in a diamond sublattice which is intertwined with the network of Bi tetrahedra. The Bi sublattice forms a hyperkagome structure as shown in Fig. 1(b).

The results from the transport measurements under magnetic field are summarized in Fig. 2. Shown in Fig. 2(a) is the electrical resistivity as a function of temperature under an applied magnetic field ranging from 0 to 9 T. At zero field, RbBi$_2$ exhibits very good metallic conductivity even at

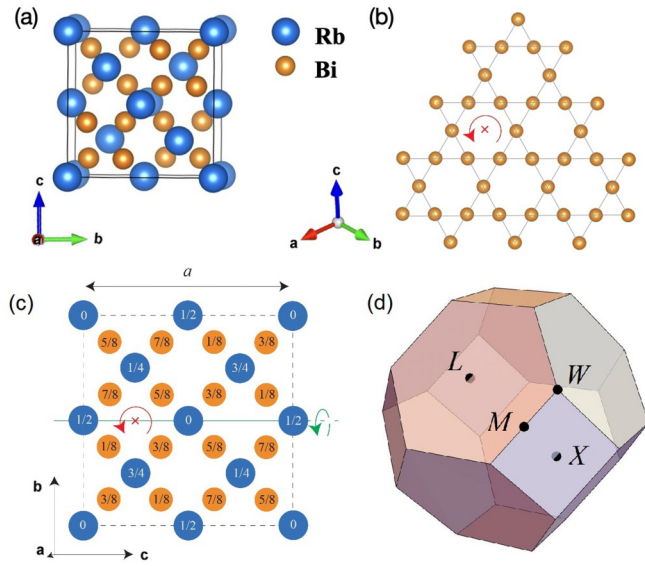*Corresponding author: louca@virginia.edu

FIG. 1. (a) The unit cell showing the cubic crystal structure of RbBi$_2$. (b) The Bi sublattice forming a hyperkagome structure on a plane perpendicular to the threefold (111) axis. (c) The fourfold screw S_4 and twofold C_2 rotations of the lattice. Number indicates the fractional part of the vertical positions of the atoms (in units of the lattice constant a). (d) Brillouin zone and high symmetry points.
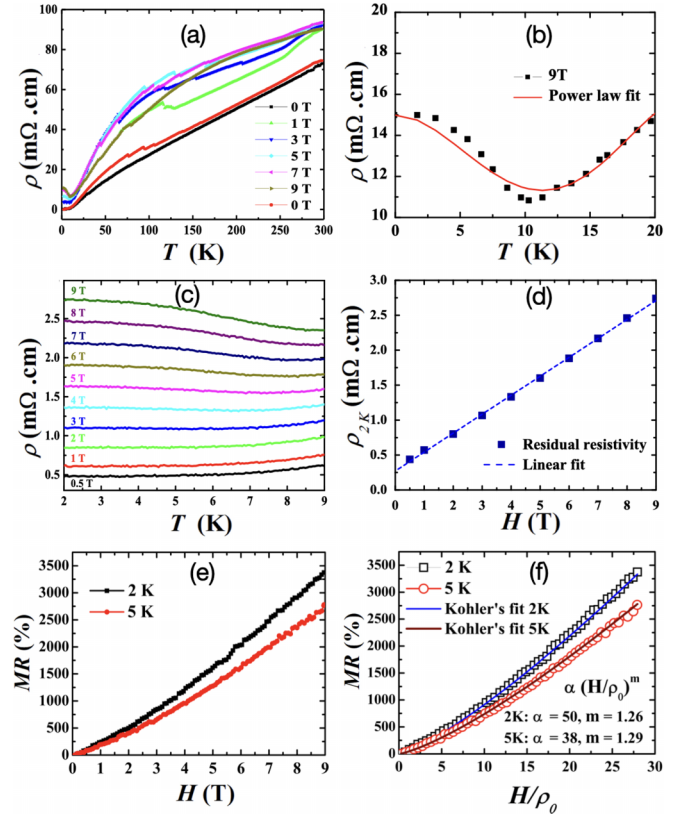

FIG. 2. (a) The electrical resistivity as a function of applied magnetic field in the range 0–9 T. (b) Temperature dependence of resistivity at low temperatures in the presence of applied field H = 9 T. The solid line shows the power law fit $\rho = \rho_0 + AT^2 + BT^3 + CT^5$ to the data at low temperatures. (c) The low temperature resistivity behavior at applied fields measured on a quenched sample of RbBi$_2$ above the critical field. (d) The residual resistivity at 2 K plotted as a function of the applied magnetic field. (e) The magnetoresistance (MR) of RbBi$_2$ is compared between data collected at 2 and 5 K. (f) MR fitted with $MR = \alpha(H/\rho_0)^m$ at 2 K and 5K showing the Kohler scaling.

room temperature. The resistivity follows a linear temperature dependence until about 25 K, below which it follows a power-law temperature dependence $\rho = A + BT^{2.91}$ as it approaches the superconducting transition. Under field, the resistivity follows a complex power law dependence. Shown in Fig. 2(b) is the resistivity as a function of temperature at 9 T. At low temperatures, the resistivity is fit (solid red line) with $\rho = \rho_0 + AT^2 + BT^3 + CT^5$ where $\rho_0 = 15, A = -0.1$, $B = 7 \times 10^{-3}$, and $C = -4.7 \times 10^{-5}$.

Below 10 K, above the critical field, H$_c$, with the superconducting transition suppressed, the resistivity exhibits a plateau that extends down to 2 K, the lowest measured temperature. The resistivity data below 10 K measured on a liquid N$_2$ quenched sample of RbBi$_2$ is shown in Fig. 2(c). The plateau is observed for fields up to 9 T, with the residual resistivity rising linearly with field [Fig. 2(d)]. The magnetic field induces a crossover in the temperature dependent behavior of the resistivity from metallic to semiconducting and is accompanied by a very large MR.

The magneto-transport behavior is shown in Fig. 2(e). The MR at two temperatures: above and below the observed T_c is plotted as a function of applied magnetic field. Typically in conventional metals, the MR decreases because the relaxation rate τ decreases with increasing temperature. The MR in this system shows no saturation at 9 T. The MR is obtained by $MR(B) = \frac{\rho(B) - \rho(B_0)}{\rho(B_0)} \times 100\%$. As-grown RbBi$_2$ exhibits an MR of about 3500% at 2 K and 9 T. The most trivial mechanism responsible for the extremely large unsaturated MR in semimetals has been associated with a semiclassical two-band model where electron and hole-like carriers are almost compensated [15]. However, nonsaturating large MR has also been observed in topological Weyl semimetals such as WTe$_2$ [16] and MoTe$_2$ [17] with high mobilities and

low-residual resistivities. Although the two-band model predicts a quadratic in applied-field MR, these systems usually exhibit a linear field dependence and the origin of the extreme MR is not well understood.

Typically the magnetotransport in semiclassical single-band metals follows a functional form known as Kohler's rule where $\Delta\rho/\rho_0 \propto F(H/\rho_0)$, in which ρ_0 is the zero-field resistivity [18]. In most simple metals, the MR exhibits an H^2 dependence so that MR is proportional to $\tau^2 H^2$. Therefore a plot of MR versus (H/ρ_0) is expected to collapse to a single temperature independent curve if the number of carriers is constant, and with only one type of carrier with a scattering rate that is the same at all points on the Fermi surface. This is not what is observed as seen from the fitting of the MR in RbBi$_2$ with Kohler's scaling [Fig. 2(f)]. $\Delta\rho/\rho_0 \propto (H/\rho_0)^{1.26}$ which is not consistent with a Fermi-liquid quasiparticle scattering rate. We suggest that the electron-hole compensation can be one potential explanation for the large MR behavior in RbBi$_2$, however, we do not see a quadratic field dependence of MR which implies that such compensation is weak. It is not
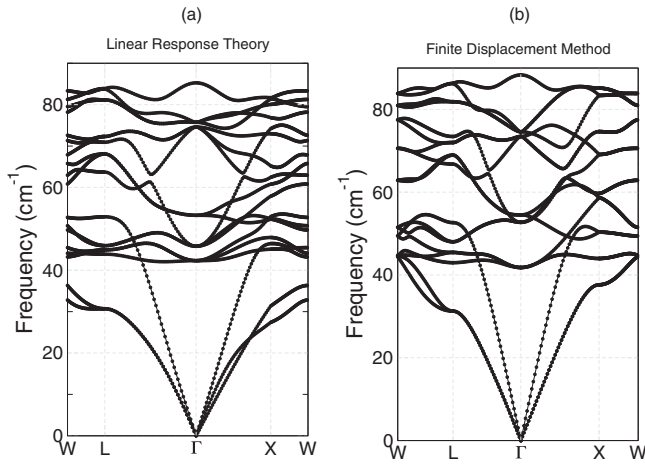
FIG. 3. Phonon dispersion curves of RbBi$_2$ along the high-symmetry directions using (a) Linear-response theory and (b) Finite displacement method. The high symmetry points are marked in the Brillouin zone in Fig. 1(d).

likely for the electron-hole compensation to be the dominant mechanism due to the complex nature of Fermi surface in this material. The different temperature dependence of ρ and MR is because ρ is related to the $1/\tau$ over the Fermi surface. The MR on the other hand is related to $\langle \tau \rangle$ over the Fermi surface. The transport and magnetotransport are reminiscent of the behavior observed in systems such as Ag$_{2-d}$(Te/Se)$_d$ [19], Bi$_2$Te$_3$ [20], Bi metal [21], graphite [22], Cd$_3$As$_2$ [23], and (Sr/Ca)MnBi$_2$ [24]. In these systems, the mechanism for the large MR has been attributed to involve the presence of Dirac fermions and their linear dispersion [such as in Ag$_{2-d}$(Te/Se)$_d$, Bi$_2$Te$_3$] or Fermi surface compensation. It is possible that the magnetic field breaks TRS and reorganizes the Dirac Fermi surface. A high mobility of the Dirac carriers could induce a very large MR as in the case of Cd$_3$As$_2$.

B. Phonons and electron-phonon coupling

The phonon dispersion curves along the W-L-Γ-X-W high symmetry points as calculated using linear-response theory [Fig. 3(a)] and the results from the supercell based finite displacement method are shown [Fig. 3(b)]. Overall, both plots show similar features. Most importantly, no phonons with imaginary frequencies are found using either method. This suggests that the cubic structure of RbBi$_2$ is dynamically stable at 0 K. This result is in agreement with the experimental data where no structural phase transition was seen in any of our experiments down to 2 K.

The calculated electron-phonon coupling constant, λ_{ep}, from the linear-response theory varied from 0.55 to 0.72 depending on the broadening used to calculate the $\alpha^2 F(\omega)$ function. Since our calculated λ_{ep} is less than one, we used the McMillan formula [13] instead of the Allen-Dynes formula to estimate T_c. The McMillan formula provided a T_c estimate between 1.263 and 2.852 K, which is in close agreement with the experimental value ($\sim$4.15 K for a polycrystal). Intriguingly, our calculated λ_{ep} for RbBi$_2$ agrees closely with that in KBi$_2$ [25], an experimentally confirmed Type-I superconductor [9].

C. Electronic band structure and Fermi surface

In Figs. 4(a) and 4(b), electronic band structures of metallic RbBi$_2$ without and with SOC are shown along the Γ-X-W-Γ-L high symmetry directions, respectively. In the absence of SOC, a total of four bands cross the Fermi energy (E$_F$). All four bands are from the Bi-atom. Introducing SOC has a nontrivial effect on the electronic band structure. Some of the major changes occur along the X-W k path near E$_F$. Two bands that cross the Γ-X and X-W k path in Fig. 4(a) are shifted to higher energies (by $\sim$0.5 eV) as shown in Fig. 4(b). Consequently, in the SOC electronic band structure, no bands cross E$_F$ along the X-W path. Another interesting difference due to SOC is observed in the W-Γ path. A Dirac-like linear dispersion along the W-Γ path at $\sim$0.75 eV below E$_F$ in Fig. 4(a) is gapped in Fig. 4(b) when SOC is turned on. The band crossing at the X point just above the Fermi level is also Dirac which is qualitatively the same as the one below the Fermi level.

Figure 5(a) is a plot of the Fermi surface without SOC. An electron pocket (in red) is located at the Γ point of the BZ. Hole pockets at the X and L points can be seen in Figs. 5(c) and (d), resulting in a complex Fermi surface with electron and hole characteristics as shown in Fig. 5(b). This topology is similar to the Fermi surface of superconductor KBi$_2$ [25]. In Fig. 6, the Fermi surface and corresponding Fermi velocity are plotted with SOC included. An electron pocket is present at the Γ point, shown in green in Fig. 6(a). In Fig. 6(b), a complex structure that consists of tubes connecting the X and L points are formed. The maximum and minimum Fermi velocities, v_f, were calculated to be 2.64×10^6 and 0.65×10^6 'm/s, respectively. The maximum v_f is found around the electron pocket in the Γ point of the BZ [Fig. 6(c)], whereas the minimum v_f is found in the tubes that connect the X and L points.

D. Massless Dirac fermions at the X points

The fourfold degenerate bands closest to and below E$_F$ at each of the three X points correspond to a massless Dirac fermion [Fig. 4(c)] [26]. Thus, RbBi$_2$ is a Dirac (semi)metal [27]. Here we review the symmetry-protected Dirac point and present an effective $\mathbf{k} \cdot \mathbf{p}$ Hamiltonian description near each X point. The symmetry group at X is generated by time reversal T, inversion P, twofold rotation C_2, and fourfold screw rotation S_4. Since the three X points are related to each other by the threefold rotation about the (111) axis, it suffices to focus on one where S_4 is parallel to, say, the **a** axis and the C_2 is parallel to the perpendicular **b** axis. [See Fig. 1(c)]. While the symmorphic C_2, P, and T all mutually commute, the nonsymmorphic screw rotation $S_4 = C_4 T_\mathbf{a}^{1/4}$ contains the fractional translation $T_\mathbf{a}^{1/4}$ and does not commute with P and C_2. $T_\mathbf{a}^{1/4}$ translates along the **a** axis by $a/4$, where a is the lattice constant of the cubic cell. At the X point, $(T_\mathbf{a}^{1/4})^2 = -1$ and therefore the screw representation obeys $PS_4P = -S_4$. The twofold rotation flips the screw direction by conjugacy, $C_2 S_4 C_2^{-1} = S_4^{-1}$.

The fourfold degenerate bands at X irreducible represents the little group and is referred to as X_5. We adopt the following 4×4 matrix representations for the symmetries. $T = is_y \mathcal{K}$
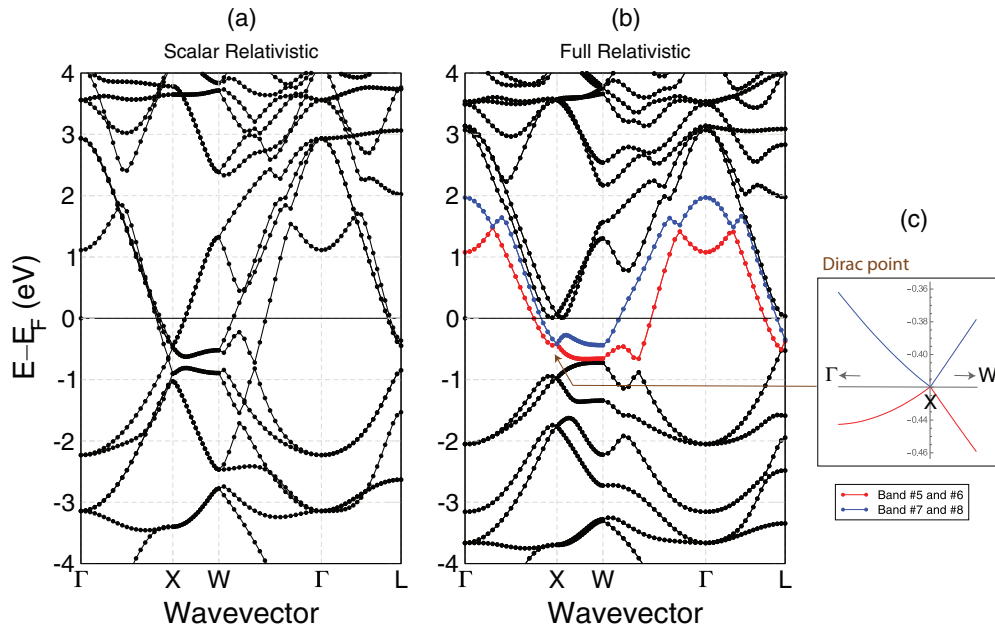
FIG. 4. Electronic band structures of RbBi$_2$ (a) without SOC (scalar relativistic) and (b) with SOC (fully relativistic). The Fermi energy (E$_F$) is set at 0 eV. (c) Dirac point at X at -0.4187 eV below the Fermi level. For the two pairs of bands that cross the Fermi level, the degenerate pair with lower (higher) energy are bands No. 5 and No. 6 (No. 7 and No. 8).

where $\mathcal{K}$ is the complex conjugate, and

$$C_2 = \begin{pmatrix} is_y & 0 \\ 0 & -is_x \end{pmatrix}, \quad S_4 = \begin{pmatrix} 0 & is_y \\ is_x & 0 \end{pmatrix}, \quad (1)$$

and $P = \sigma_z = \text{diag}(1, -1)$. Here, $s_{x,y,z}$ are the spin Pauli matrices, and 1 is the spin identity matrix. The Kramers' theorem and PT symmetry, which is antiunitary and squares to $(PT)^2 = -1$, requires all band at all momentum to be doubly degenerate. Restricting to the screw symmetric

a axis in momentum space, bands can be labeled by their S_4 eigenvalues. The four bands near the Dirac point along $k_{\mathbf{a}}$ are grouped in two degenerate pairs with S_4 eigenvalues $\{e^{i\pi/4}, e^{i3\pi/4}\}$ and $\{e^{-i\pi/4}, e^{-i3\pi/4}\}$. The eigenvalues are 4th roots of unity because $S_4^4 = -1$. PT switches the degenerate eigenstates since $(PT)S_4 = -S_4(PT)$. For
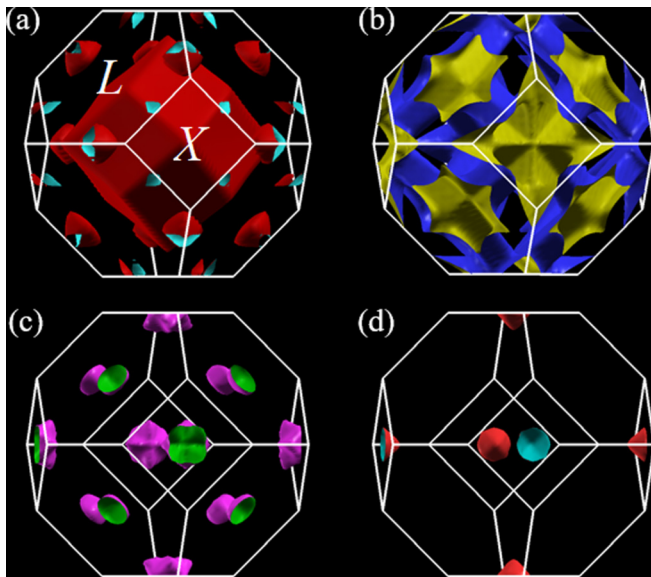

FIG. 5. (a)–(d) Fermi surface without SOC for RbBi$_2$. Four bands cross the E$_F$, whose Fermi surface is shown here. The Brillouin zone showing the high symmetry points is shown in Fig. 1(d).
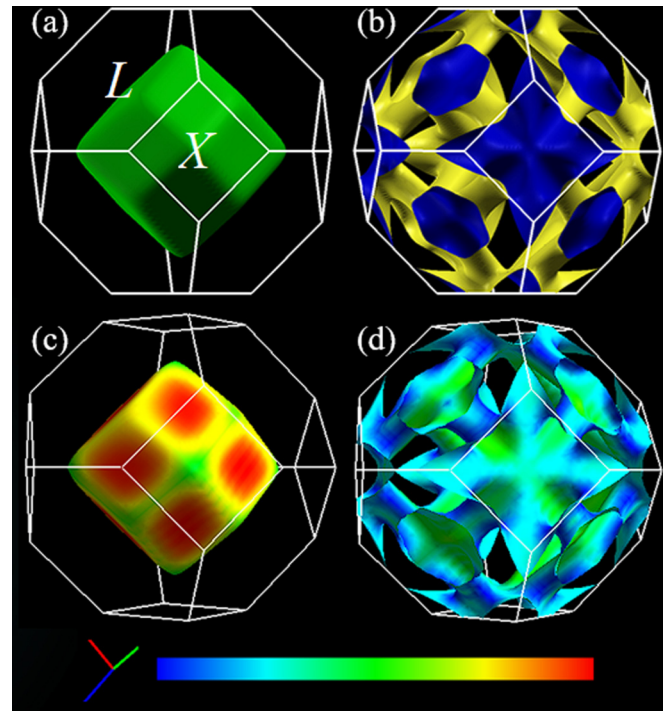

FIG. 6. (a)–(d) Fermi surface and corresponding Fermi velocity of RbBi$_2$ with SOC. The high symmetry points are labeled.

example, $S_4(PT)|e^{i\pi/4}\rangle = -(PT)S_4|e^{i\pi/4}\rangle = -(PT)e^{i\pi/4}|e^{i\pi/4}\rangle = e^{i3\pi/4}(PT)|e^{i\pi/4}\rangle$. These two pairs of degenerate bands cross at X and the Dirac crossing is protected by S_4 and PT symmetry.

The massless Dirac bands can be effectively described by the $\mathbf{k} \cdot \mathbf{p}$ Hamiltonian in a linear approximation near the X point,

$$H(X + \mathbf{k}) = \epsilon_X \mathbb{I} + \hbar v_z k_z \gamma_z + \hbar v_x (k_x \gamma_x + k_y \gamma_y), \quad (2)$$

where the x, y, z directions are the orthogonal b, c, a directions, respectively. The fourfold degenerate bands at X sits below E_F at $\epsilon_X = -0.418705$ eV. The gamma matrices are restricted by the little symmetry group at X_5. They are

$$\gamma_z = \frac{\sigma_x(s_x + s_y)}{\sqrt{2}}, \quad \gamma_x = \frac{\sigma_y + \sigma_x s_z}{\sqrt{2}}, \quad \gamma_y = \frac{\sigma_y - \sigma_x s_z}{\sqrt{2}}, \quad (3)$$

which mutually anticommute, and each matrix square equals to the identity, $\gamma^2 = \mathbb{I}$. The Fermi velocities v_x and v_z along the axis normal and parallel to the screw direction from X are extracted by a polynomial fit of band energies near X (within 4% away from X towards Γ and M). Using the numerical lattice parameter $a = 9.52016$ Å, they are $v_x = (2.568 \pm 0.006) \times 10^5$ m/s and $v_z = (4.94 \pm 0.06) \times 10^5$ m/s.

The Dirac fermions at the three X points can become massive if the fourfold screw symmetry is broken, for example when the material is under uniaxial stress along the threefold (111) direction. The only timereversal and inversion symmetric mass term is mP, where the Dirac masses of the three X points are identical due to the threefold symmetry. The sign of m depends on the sign of stress. Since the tension and compression phases are separated by three Dirac transitions—an odd number, one of them must be in the strong $\mathbb{Z}_2$ topological insulating phase, and exhibits gapless Dirac surface bands at the surface projected $\bar{X}$ points.

E. Topology of the Fermi surfaces

Although RbBi₂ has finite Fermi surfaces and is a band metal, it is classified as an enforced semimetal with Fermi degeneracy (ESFD) [28] for the following reasons. The partially filled doubly degenerate conduction bands No. 7 and No. 8 can be continuously deformed above E_F while keeping all symmetries (see Fig. 4). Similarly, the partially empty doubly degenerate valence bands No. 5 and No. 6 can be moved below E_F. The Dirac crossing at X between the conduction and valence bands is still symmetry protected. It will reside exactly at the Fermi level after a continuous band deformation because of charge neutrality and electron filling. The resulting band structure is semimetallic as it has a vanishing Fermi surface and energy gap. However, in the real material, the electron and hole pockets have finite Fermi surfaces. They enclose the same volume in momentum space because of charge neutrality.

The valence bands No. 5 and No. 6 cut across E_F and give rise to the hole pocket Fermi surface [shown in Fig. 6(a)]. It has an isotropic shape and resembles a smoothed out rhombic dodecahedron that encloses the Γ point at its center. The conduction bands No. 7 and No. 8 cut across E_F and give rise to the electron pocket Fermi surface [shown in Fig. 6(b)].

At low temperature, the electron pocket occupies regions near the boundary of the Brillouin zone including the X and L points, and does not overlap with the hole pocket near the zone center. The electron Fermi surface Σ_{e-FS} has genus 18, and is topologically equivalent to a torus with 18 "holes". It has 18 independent longitudinal cycles that wrap inside Σ_{e-FS} where the conduction band is occupied, and 18 meridian cycles that wrap outside Σ_{e-FS} where the conduction band is empty. The electron Fermi surface Σ_{e-FS} consists of 24 "tubes" that connect between the three X points and the four L points. Each X point is connected to any given L point by two "tubes". The longitudinal (meridian) cycles run inside (outside) the tubes. A longitudinal loop cycle links a meridian cycle if they thread the same tube. We defer the consequence of the negative Gaussian curvature of Σ_{e-FS} and the Wilson loop algebra of its cycles to future work.

III. CONCLUSION AND SPECULATION

There exists a large list of nonmagnetic compounds recently discovered that exhibit extraordinary responses under field, i.e., large positive MR, with centrosymmetric symmetries. Systems such as NbSb₂ [29], YSb [30], LaSb [31], MoAs₂ [10], TaSb₂ [32], and NbAs₂ [33] all show strong MR, a resistivity plateau, induced by the magnetic field, leading to a crossover from a metal to a semiconductor. In these systems, the exponent in the Kohler's fitting is less than two, indicating weaker carrier compensation. Magnetotransport in semiclassical single-band metals scales as MR $= F(H/\rho_0)$ assuming a single scattering rate. In our system, MR $\propto H^{1.26}$ which deviates from Kohler scaling. The MR is almost linear that may arise from the quantum limit, suggesting that it could be the Dirac carriers that induce the large MR [34].

We close by speculating on the prospect of normal metallic and superconducting phases of this Dirac material under symmetry-breaking perturbations. The three massless Dirac fermions can become massive in this case and RbBi₂ may serve as a testbed for tunable topological phases. As discussed in Sec. II D, we expect uniaxial stress along the (111) direction turn the material into a strong topological insulator that hosts protected surface Dirac fermions. It would be equally interesting to explore the effects of other directional perturbations such as electric/magnetic fields or shear stress, on the topology and transport nature of this system. The high genus electron Fermi surface contains saddle point regions with negative Gaussian curvature that associate to high density of states and locally flat energy dispersions along special directions. These regions are prone to electron many-body interactions and may give rise to nontrivial strong correlated behaviors. The superconducting state of RbBi₂ deserves further investigation due to the strong SOC and Dirac nature of the material. For example, the surface Dirac fermion of a topological insulator are known to host vortex-bound Majorana zero modes under superconducting pairing [35]. Although RbBi₂ is a type-I superconductor, quantum vortices could be introduced in thin film sandwiched by bulk trivial type-II superconductors. It would be interesting to observe such exotic excitations on the superconducting RbBi₂ surface and the onset of surface Majorana gap under a strong enough symmetry-lowering perturbation such as the uniaxial stress.

Thus, $RbBi_2$ is a strong candidate to be a topological system from which the interplay of superconductivity and Dirac states can be explored.

Methods

1. Material Synthesis

The $RbBi_2$ samples were prepared by solid state reaction following the procedure described in Ref. [14]. Rubidium pieces (Alfa Aesar, 99.5%) and Bismuth powder (Alfa Aesar, 99.99%) were mixed in a 1:2 molar ratio and the mixture was vacuum sealed in a quartz ampule. The samples were heated at $700\,^{\circ}C$ for 24 hours. Two batches of samples were synthesized, one that was slowly cooled down (furnacecooled) to room temperature and the other quenched from $700\,^{\circ}C$ in liquid N_2 to room temperature. The samples are denoted as AG (as-grown) and Q (quenched), respectively. The sample preparation and handling were done inside an Argon filled glovebox to avoid exposure to air. Electrical transport and magnetization measurements were performed as a function of magnetic field. Magnetic field studies on correlated metals have been instrumental in revealing the ground state properties of the normal state by suppressing the superconducting transition. The magnetic field interacts with the charge carriers through the Lorentz force, coupling directly to the orbital motion.

2. First Principles Calculations

DFT calculations were performed using the planewave pseudopotential code, QUANTUM ESPRESSO [36] within the generalized gradient approximation [37] and the PBEsol exchange-correlation functional is used for all calculations [38]. The ultrasoft pseudopotential optimized in the Rappe-Rabe-Kaxiras-Joannopoulos scheme was used to treat the core and valence electrons [39]. The $RbBi_2$ system is built as a six-atom cubic cell (space group $Fd\bar{3}m$), where Rb atoms occupy the $8a$ Wyckoff site and the Bi atoms occupy the $16d$ site. The lattice constant was obtained by performing a variable-cell optimization, where both the cell and the internal coordinates were allowed to relax. A Γ point centered Monkhorst-Pack k-point mesh of size $16 \times 16 \times 16$ was used

for the structure optimization [40]. A kinetic energy and charge density cutoff of 70 and 700 Ry, respectively, were used in the self-consistent field (SCF) calculation. An energy threshold of 7×10^{-10} Ry was used for the SCF calculation in the electronic steps. Marzari-Vanderbilt smearing with a degauss width of 0.001 Ry was used [41]. The calculated equilibrium lattice parameter of 9.52016 Å agreed well with the experimental value (9.59 Å). The electronic band structure and Fermi surface calculations were performed with and without SOC in the Hamiltonian. In the SOC calculations, fully-relativistic pseudopotential were used only for the Bi-atoms because the atom-projected density of states indicated that only the Bi-orbitals are involved in the Fermi surface. For the Fermi surface calculations, non-SCF calculations were performed with a dense $32 \times 32 \times 32$ k mesh. The Fermi surface is visualized using XCRYSDEN [42]. The Fermi velocity was also calculated using the SOC term (v_f) and visualized the contour using the Fermisurfer software [43].

The phonon dispersion curve, electron-phonon coupling strength (λ_{ep}), and Eliashberg spectral function [$\alpha^2 F(\omega)$] were calculated using the linear-response theory [44]. Both Rb and Bi atoms are described using scalar-relativistic pseudopotentials in these calculations. The superconducting critical temperature was calculated using the McMillan formula [13]. An energy threshold of 10^{-15} Ry was used for self-consistency based on a $4 \times 4 \times 4$ Monkhorst-Pack grid. A total of ten double-delta smearing values with a spacing of 0.005 Ry were used in the electron-phonon coupling calculation. In addition to the linear-response theory, the phonon dispersion curve was also calculated based on the finite displacement method using PHONOPY [45]. A $2 \times 2 \times 2$ supercell of the conventional cell was used in these calculations. In the SCF calculations, a $4 \times 4 \times 4$ k point mesh and an energy threshold of 7×10^{-12} Ry were used for convergence.

[1] C. L. Kane and E. J. Mele, Quantum Spin Hall Effect in Graphene, Phys. Rev. Lett. **95**, 226801 (2005).

[2] L. Fu, C. L. Kane, and E. J. Mele, Topological Insulators in Three Dimensions, Phys. Rev. Lett. **98**, 106803 (2007).

[3] J. M. Reynolds and C. T. Lane, Superconducting bismuth alloys, Phys. Rev. **79**, 405 (1950).

[4] B. W. Roberts, Survey of superconductive materials and critical evaluation of selected properties, J. Phys. Chem. Ref. Data **5**, 581 (1976).

[5] M. Sturza, F. Han, C. D. Malliakas, D. Y. Chung, H. Claus, and M. G. Kanatzidis, Superconductivity in the intermetallic pnictide compound $Ca_{11}Bi_{10-x}$, Phys. Rev. B **89**, 054512 (2014).

[6] F Merlo and M. L. Fornasini, Crystal structure of some phases and alloying behaviour in alkaline earths, europium and ytterbium pnictides, Mater. Res. Bull. **29**, 149 (1994).

[7] B. T. Matthias and J. K. Hulm, A search for new superconducting compounds, Phys. Rev. **87**, 799 (1952).

[8] A. Iyo, Y. Yanagi, S. Ishida, K. Oka, Y. Yoshida, K. Kihou, C. H. Lee, H. Kito, N. Takeshita, I. Hase *et al.*, Superconductivity at 4.4 k in Ba_2Bi_3, Supercond. Sci. Technol. **27**, 072001 (2014).

[9] S. Sun, K. Liu, and H. Lei, Type-i superconductivity in KBi_2 single crystals, J. Phys.: Condens. Matter **28**, 085701 (2016).

[10] J. Wang, L. Li, W. You, T. Wang, C. Cao, J. Dai, and Y. Li, Magnetoresistance and robust resistivity plateau in $MoAs_2$, Sci. Rep. **7**, 1 (2017).

[11] M. K. Chan, M. J. Veit, C. J. Dorow, Y. Ge, Y. Li, W. Tabis, Y. Tang, X. Zhao, N. Barišić, and M. Greven, In-Plane Magnetoresistance Obeys Kohler's Rule in the Pseudogap Phase of Cuprate Superconductors, Phys. Rev. Lett. **113**, 177005 (2014).

[12] M. Kohler, To the magnetic resistance a change of pure metals, Ann. Phys. **424**, 211 (1938).

[13] W. L. McMillan, Transition temperature of strong-coupled superconductors, Phys. Rev. **167**, 331 (1968).

[14] S. S. Philip, J. Yang, D. Louca, P. F. S. Rosa, J. D. Thompson, and K. L. Page, Bismuth kagome sublattice distortions by quenching and flux pinning in superconducting RbBi$_2$, Phys. Rev. B **104**, 104503 (2021).

[15] N. H. Jo, Y. Wu, L.-L. Wang, P. P. Orth, S. S. Downing, S. Manni, D. Mou, D. D. Johnson, A. Kaminski, S. L. Bud'ko *et al.*, Extremely large magnetoresistance and kohler's rule in PdSn$_4$: A complete study of thermodynamic, transport, and band-structure properties, Phys. Rev. B **96**, 165145 (2017).

[16] M. N. Ali, J. Xiong, S. Flynn, J. Tao, Q. D. Gibson, L. M. Schoop, T. Liang, N. Haldolaarachchige, M. Hirschberger, N. P. Ong *et al.*, Large, non-saturating magnetoresistance in WTe$_2$, Nature (London) **514**, 205 (2014).

[17] Q. L. Pei, X. Luo, F. C. Chen, H. Y. Lv, Y. Sun, W. J. Lu, P. Tong, Z. G. Sheng, Y. Y. Han, W. H. Song *et al.*, Mobility spectrum analytical approach for the type-ii weyl semimetal T_d-MoTe$_2$, Appl. Phys. Lett. **112**, 072401 (2018).

[18] J. M. Ziman, *Electrons and Phonons: The Theory of Transport Phenomena in Solids* (Oxford University Press, Oxford, 2001).

[19] R. Xu, A. Husmann, T. F. Rosenbaum, M.-L. Saboungi, J. E. Enderby, and P. B. Littlewood, Large magnetoresistance in non-magnetic silver chalcogenides, Nature (London) **390**, 57 (1997).

[20] X. Wang, Y. Du, S. Dou, and C. Zhang, Room Temperature Giant and Linear Magnetoresistance in Topological Insulator Bi$_2$Te$_3$ Nanosheets, Phys. Rev. Lett. **108**, 266806 (2012).

[21] F. Y. Yang, K. Liu, K. Hong, D. H. Reich, P. C. Searson, and C. L. Chien, Large magnetoresistance of electrodeposited single-crystal bismuth thin films, Science **284**, 1335 (1999).

[22] K. Noto and T. Tsuzuku, Kohler's rule for magnetoresistance of graphite and carbons, Carbon **12**, 209 (1974).

[23] L. P. He, X. C. Hong, J. K. Dong, J. Pan, Z. Zhang, J. Zhang, and S. Y. Li, Quantum Transport Evidence for the Three-Dimensional Dirac Semimetal Phase in Cd$_3$As$_2$, Phys. Rev. Lett. **113**, 246402 (2014).

[24] J. Park, G. Lee, F. Wolff-Fabris, Y. Y. Koh, M. J. Eom, Y. K. Kim, M. A. Farhan, Y. J. Jo, C. Kim, J. H. Shim, and J. S. Kim, Anisotropic Dirac Fermions in a Bi Square Net of SrMnBi$_2$, Phys. Rev. Lett. **107**, 126402 (2011).

[25] J. Chen, A comprehensive investigation of superconductor KBi$_2$ via first-principles calculations, J. Supercond. Novel Magn. **31**, 1301 (2018).

[26] P. A. M. Dirac, The quantum theory of the electron, Proc. R. Soc. London A **117**, 610 (1928).

[27] O. Vafek and A. Vishwanath, Dirac fermions in solids: From high-tc cuprates and graphene to topological insulators and weyl semimetals, Annu. Rev. Condens. Matter Phys. **5**, 83 (2014).

[28] B. Bradlyn, L. Elcoro, J. Cano, M. G. Vergniory, Z. Wang, C. Felser, M. I. Aroyo, and B. A. Bernevig, Topological quantum chemistry, Nature (London) **547**, 298 (2017).

[29] K. Wang, D. Graf, L. Li, L. Wang, and C. Petrovic, Anisotropic giant magnetoresistance in NbSb$_2$, Sci. Rep. **4**, 7328 (2014).

[30] O. Pavlosiuk, P. Swatek, and P. Wiśniewski, Giant magnetoresistance, three-dimensional fermi surface and origin of resistivity plateau in ysb semimetal, Sci. Rep. **6**, 1 (2016).

[31] F. F. Tafti, Q. D. Gibson, S. K. Kushwaha, N. Haldolaarachchige, and R. J. Cava, Resistivity plateau and extreme magnetoresistance in LaSb, Nat. Phys. **12**, 272 (2016).

[32] Y. Li, L. Li, J. Wang, T. Wang, X. Xu, C. Xi, C. Cao, and J. Dai, Resistivity plateau and negative magnetoresistance in the topological semimetal TaSb$_2$, Phys. Rev. B **94**, 121115(R) (2016).

[33] Z. Yuan, H. Lu, Y. Liu, J. Wang, and S. Jia, Large magnetoresistance in compensated semimetals TaAs$_2$ and NbAs$_2$, Phys. Rev. B **93**, 184405 (2016).

[34] A. A. Abrikosov, Quantum magnetoresistance, Phys. Rev. B **58**, 2788 (1998).

[35] L. Fu and C. L. Kane, Superconducting Proximity Effect and Majorana Fermions at the Surface of a Topological Insulator, Phys. Rev. Lett. **100**, 096407 (2008).

[36] P. Giannozzi, S. Baroni, N. Bonini, M. Calandra, R. Car, C. Cavazzoni, D. Ceresoli, G. L. Chiarotti, M. Cococcioni, I. Dabo *et al.*, Quantum espresso: A modular and open-source software project for quantum simulations of materials, J. Phys.: Condens. Matter **21**, 395502 (2009).

[37] J. P. Perdew, K. Burke, and M. Ernzerhof, Generalized Gradient Approximation Made Simple, Phys. Rev. Lett. **77**, 3865 (1996).

[38] J. P. Perdew, A. Ruzsinszky, G. I. Csonka, O. A. Vydrov, G. E. Scuseria, L. A. Constantin, X. Zhou, and K. Burke, Restoring the Density-Gradient Expansion for Exchange in Solids and Surfaces, Phys. Rev. Lett. **100**, 136406 (2008).

[39] D. Vanderbilt, Soft self-consistent pseudopotentials in a generalized eigenvalue formalism, Phys. Rev. B **41**, 7892 (1990).

[40] H. J. Monkhorst and J. D. Pack, Special points for Brillouin-zone integrations, Phys. Rev. B **13**, 5188 (1976).

[41] N. Marzari, D. Vanderbilt, A. De Vita, and M. C. Payne, Thermal Contraction and Disordering of the Al(110) Surface, Phys. Rev. Lett. **82**, 3296 (1999).

[42] A. Kokalj, Xcrysden-a new program for displaying crystalline structures and electron densities, J. Mol. Graphics Modell. **17**, 176 (1999).

[43] M. Kawamura, FermiSurfer: Fermi-surface viewer providing multiple representation schemes, Comput. Phys. Commun. **239**, 197 (2019).

[44] S. Baroni, S. de Gironcoli, A. Dal Corso, and P. Giannozzi, Phonons and related crystal properties from density-functional perturbation theory, Rev. Mod. Phys. **73**, 515 (2001).

[45] A. Togo and I. Tanaka, First principles phonon calculations in materials science, Scr. Mater. **108**, 1 (2015).